

Establishing the Dependence of $[\text{HO}_2]/[\text{OH}]$ on Temperature, Halogen Loading, O_3 , and NO_x Based on in Situ Measurements from the NASA ER-2[†]

E. J. Lanzendorf,^{*,‡} T. F. Hanisco,[‡] P. O. Wennberg,[§] R. C. Cohen,[⊥] R. M. Stimpfle,[‡]
J. G. Anderson,[‡] R. S. Gao,[¶] J. J. Margitan,[§] and T. P. Bui[#]

Department of Chemistry and Chemical Biology, Harvard University, Cambridge, Massachusetts 02138; Division of Geological and Planetary Sciences and Division of Engineering, California Institute of Technology, Pasadena, California 91125; Department of Chemistry, University of California—Berkeley, Berkeley, California 94720; National Oceanic and Atmospheric Administration Aeronomy Laboratory, Boulder, Colorado 80303; Jet Propulsion Laboratory, California Institute of Technology, Pasadena, California 91109; and NASA Ames Research Center, Moffett Field, California 94035

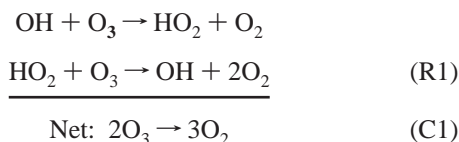
Received: July 3, 2000; In Final Form: October 18, 2000

In situ observations of OH and HO₂ from the Airborne Southern Hemisphere Ozone Experiment/Measurements for Assessing the Effects of Stratospheric Aircraft (ASHOE/MAESA), Stratospheric TRacers of Atmospheric Transport (STRAT), and Polar Ozone Loss in the Arctic Region in Summer (POLARIS) NASA ER-2 field campaigns are used to examine the partitioning of HO_x in the lower stratosphere (tropopause to ~21 km) and upper troposphere (~10 km to tropopause). These measurements span a latitude range from 70°S to 90°N and a variety of atmospheric conditions as a result of seasonal changes and altitude. The response of the observed $[\text{HO}_2]/[\text{OH}]$ to changes in temperature, $[\text{O}_3]$, $[\text{CO}]$, $[\text{NO}]$, $[\text{ClO}]$, and $[\text{BrO}]$ is investigated. The measured ratio is accurately described ($\sim\pm 10\%$) by a steady-state model constrained by the measured mixing ratios of O₃, CO, NO, ClO, and BrO, where the model is valid for conditions of HO_x cycling much faster than HO_x production and loss. The concentration of HO₂ depends on [OH], which, to first order, has been observed to be a simple function of the solar zenith angle in the lower stratosphere.¹ The partitioning between OH and HO₂ is controlled by the local chemistry between the HO_x radicals and O₃, CO, NO, ClO, and BrO. The response of $[\text{HO}_x]$ to changes in $[\text{NO}_x]$ and $[\text{O}_3]$ is demonstrated. Further observations are necessary to illustrate the response of HO_x to changes in halogen concentrations. A quantitative understanding of $[\text{HO}_2]/[\text{OH}]$ is important, since many of the reactions that control this ratio are directly involved in catalytic removal of O₃ in the lower stratosphere and production of O₃ in the upper troposphere.

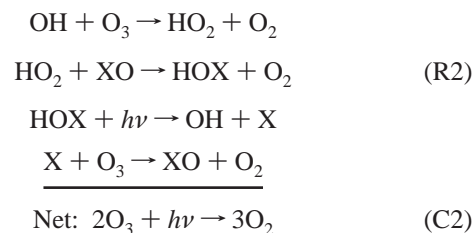
Introduction

In both the lower stratosphere and upper troposphere, the mixing ratios of HO_x (OH + HO₂) radicals are small, with OH typically less than a few parts per trillion by volume (pptv) and HO₂ typically a factor of 4–5 larger. Despite their low mixing ratios, the high reactivity of HO_x radicals makes them central to the photochemistry of both the stratosphere and troposphere.^{2,3} In particular, HO_x plays an important role in the removal mechanisms of O₃ in the lower stratosphere and production mechanism of O₃ in the upper troposphere.

In the lower stratosphere, many of the reactions that cycle HO_x constitute pathways for the catalytic removal of O₃. The reaction of OH and HO₂ with ozone constitutes a catalytic ozone removal cycle



where R1 is the rate-limiting reaction in this cycle. Additionally, HO_x cycling causes removal of O₃ by coupled reactions with halogen species (X = Cl or Br) by the following cycles that are catalytic in both halogen and hydroxyl radicals



[†] Part of the special issue "Harold Johnston Festschrift".

* Corresponding author. Phone: 617-495-5922. Fax: 617-495-4902. E-mail: lanzendorf@huarp.harvard.edu.

[‡] Harvard University.

[§] Division of Geological and Planetary Sciences and Division of Engineering, California Institute of Technology.

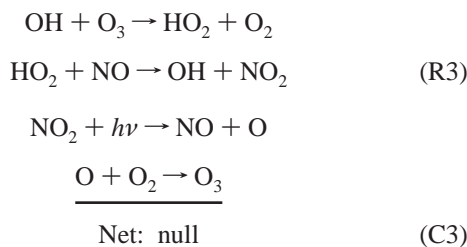
[⊥] University of California—Berkeley.

[¶] National Oceanic and Atmospheric Administration Aeronomy Laboratory.

[§] Jet Propulsion Laboratory, California Institute of Technology.

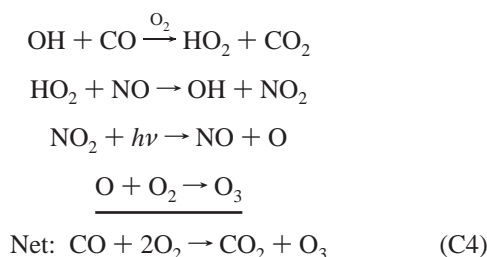
[#] NASA Ames Research Center.

Not all HO_x cycles remove ozone. The principal HO_x null cycle with respect to ozone destruction is



Reaction cycles C1–C3 are each initiated by the reaction of $\text{OH} + \text{O}_3$. This reaction depends on the OH production rate (which is highly variable)¹ and $[\text{O}_3]$. Whether or not O_3 loss happens due to HO_x partitioning depends on the branching between C1, C2, and C3 after this initiation reaction. Fundamentally, for O_3 loss from HO_x cycling to occur, the initiation reaction $\text{OH} + \text{O}_3$ is necessary. In the limit that $[\text{NO}] \rightarrow 0$, all HO_x cycling results in ozone loss.

The reaction of $\text{HO}_2 + \text{NO}$ can also lead to ozone production from the oxidation reaction of CO and other hydrocarbons. Because the concentration of CO, CH_4 , and other hydrocarbons is small in the lower stratosphere, O_3 production by HO_x cycling reactions is significant only in the troposphere. Only the catalytic cycle for CO oxidation will be considered because the production of ozone from other hydrocarbons is typically small in the upper troposphere.⁴ This cycle is catalytic in NO_x and HO_x :



Although cycling between OH and HO_2 occurs by numerous other reactions,^{5,6} the partitioning of HO_x in the lower stratosphere and upper troposphere is essentially described by the reactions found in the catalytic O_3 loss and production cycles listed above.^{7,8} At high halogen concentrations, the reaction $\text{OH} + \text{ClO} \rightarrow \text{HO}_2 + \text{Cl}$ needs to be included in HO_x interconversion processes for completeness. The reactions representing HO_x partitioning are summarized in Table 1. Generally, interconversion of OH and HO_2 in these reactions is rapid, occurring much faster than either HO_x production or loss.^{8,9} Thus, HO_x partitioning can be modeled accurately without considering influences from HO_x production and loss. An expression for the ratio, utilizing the reactions in Table 1, is given by

$$\frac{[\text{HO}_2]}{[\text{OH}]} \approx \frac{k_{\text{OH}+\text{O}_3}[\text{O}_3] + k_{\text{OH}+\text{CO}}[\text{CO}] + k_{\text{OH}+\text{ClO}}[\text{ClO}]}{k_{\text{HO}_2+\text{O}_3}[\text{O}_3] + k_{\text{HO}_2+\text{NO}}[\text{NO}] + k_{\text{HO}_2+\text{ClO}}[\text{ClO}] + k_{\text{HO}_2+\text{BrO}}[\text{BrO}]} \quad (1)$$

Throughout most of the lower stratosphere, eq 1 can be simplified to terms that only include reactions of HO_x with O_3 and NO. However, under conditions of a processed polar vortex, as the concentration of halogen species increases, reactions of HO_x with halogens become much more significant, while reactions with NO become less significant. Therefore, in the lower stratosphere, reaction cycles C1, C2, and C3 along with $\text{OH} + \text{ClO}$ accurately describe HO_x partitioning. In the upper tropo-

TABLE 1: HO_x Partitioning Reactions

conversion of $\text{OH} \rightarrow \text{HO}_2$	conversion of $\text{HO}_2 \rightarrow \text{OH}$
$\text{OH} + \text{O}_3 \rightarrow \text{HO}_2 + \text{O}_2$	$\text{HO}_2 + \text{O}_3 \rightarrow \text{OH} + 2\text{O}_2$
$\text{OH} + \text{CO} \xrightarrow{\text{O}_2} \text{HO}_2 + \text{CO}_2$	$\text{HO}_2 + \text{NO} \rightarrow \text{OH} + \text{NO}_2$
	$\text{HO}_2 + \text{ClO} \rightarrow \text{HOCl} + \text{O}_2$
	$\text{HOCl} + h\nu \rightarrow \text{OH} + \text{Cl}$
	$\text{HO}_2 + \text{BrO} \rightarrow \text{HOBr} + \text{O}_2$
	$\text{HOBr} + h\nu \rightarrow \text{OH} + \text{Br}$

sphere, the nature of the chemistry that occurs because of HO_x cycling is completely different from that in the stratosphere. High concentrations of CO and low concentrations of O_3 cause the oxidation of carbon monoxide to be the dominant HO_x cycling reaction. Therefore, reaction cycle C4 describes the exchange of OH and HO_2 to a significant level of accuracy. The HO_x partitioning reactions switch from being a mechanism for ozone removal in the lower stratosphere to being a mechanism for the catalytic production of ozone in the upper troposphere.

One of the remarkable aspects of OH photochemistry in the lower stratosphere is that $[\text{OH}]$ depends, to first order, only on solar zenith angle (SZA) and is largely independent of other chemical and dynamical variables.^{1,3} In contrast, $[\text{HO}_2]$ shows much greater variability with concentrations of other species in the lower stratosphere. Thus, the ratio of $[\text{HO}_2]$ to $[\text{OH}]$ directly describes the coupling of HO_2 concentrations to $[\text{NO}]$, $[\text{O}_3]$, $[\text{CO}]$, [halogen], and (through the reaction rate constants) temperature. The response of HO_x to photochemical changes in the lower stratosphere is observed in $[\text{HO}_2]/[\text{OH}]$. Understanding the chemistry of OH and HO_2 , therefore, is crucial for comprehending ozone loss in the lower stratosphere and ozone production in the upper troposphere.

In this work, $[\text{HO}_2]/[\text{OH}]$ (in combination with the dynamic range in the concentrations on the right-hand side of eq 1) is utilized to show that the reactions involved in the partitioning of OH and HO_2 in both the upper troposphere and lower stratosphere are accurately described by the mechanisms in the above catalytic cycles. These mechanisms include the rate-limiting steps for (1) the direct removal of O_3 by HO_x in the lower stratosphere, (2) the indirect removal of O_3 by HO_x reactions with halogens in the lower stratosphere, and (3) the production of O_3 in the upper troposphere. The quality of the agreement between the measured and modeled ratios reflects our current understanding of each of the terms in eq 1. In addition, our ability to understand how perturbations to the stratosphere affecting O_3 loss through HO_x is examined.

Measurements

The in situ measurements presented here were obtained during the 1994 to 1997 NASA ER-2 aircraft field campaigns. The Airborne Southern Hemisphere Ozone Experiment/Measurements for Assessing the Effects of Stratospheric Aircraft (ASHOE/MAESA) mission was deployed from Christchurch, New Zealand (44°S, 172°E), in 1994. This series of flights provided the first measurements of HO_x in the Antarctic region during winter. The Stratospheric TRacers of Atmospheric Transport (STRAT) campaign was deployed from Barbers Point, HI (21°N, 155°W), and Moffett Field, CA (37°N, 122°W), in 1996. These flights provided the first extensive measurements of HO_x in the upper troposphere (from 10 km to the tropopause). Most of the tropospheric data between 10 km and the tropopause was obtained within 5° latitude of Barber's Point and Moffett Field. The Polar Ozone Loss in Arctic Region in Summer (POLARIS) mission was deployed from Fairbanks, Alaska

TABLE 2: Measurements on NASA ER-2 Used for HO_2/OH Analysis

species	measurement technique	uncertainty ^a	ref
OH	laser induced fluorescence	$\pm 25\% \pm 0.01$ ppt (2σ)	Wennberg et al. ¹⁰
HO_2	laser induced fluorescence	$\pm 30\% \pm 0.02$ ppt (2σ)	Wennberg et al. ¹⁰
O_3	UV absorption	$\pm 5\%$	Proffitt et al. ¹¹
NO	chemiluminescence	$\pm 6\% \pm 4$ pptv (1σ)	Fahey et al. ¹²
CO	tunable diode laser absorption spectroscopy	$\pm 10\%$ (1σ)	Webster et al. ¹³
ClO	chemical conversion/resonance fluorescence	$\pm 15\%$	Brune et al. ¹⁵
BrO	chemical conversion/resonance fluorescence	$\pm 15\%$	Brune et al. ¹⁴
pressure (mbar)		± 0.25 mbar	Chan et al. ¹⁶
temp (K)		± 0.3 K	Chan et al. ¹⁶

^a When given, both the percentage and the value in pptv must be utilized to calculate the estimated systematic uncertainties.

(65°N, 148°W), in 1997. Measurements of HO_x , NO_x , and ClO in the Arctic summer provided a unique opportunity to examine the photochemistry of the radicals responsible for both catalytic destruction of O_3 in the stratosphere and production in the upper troposphere under constant solar illumination. Collectively, these observations span large variations in atmospheric conditions, having been obtained during all four seasons and over a wide range of altitude (10–21 km) and latitude (from 70°S to 90°N).

The experimental measurement of OH and HO_2 on the ER-2 research aircraft is described in detail by Wennberg et al.¹⁰ OH is measured by laser induced fluorescence (LIF) with an accuracy of $\pm 25\%$ (2σ) and an instrument precision of $\pm 1 \times 10^4$ molecules/ cm^3 (typically $\sim 1\%$) for a 1 min averaging period. HO_2 is measured by chemical conversion to OH using NO, with the OH subsequently detected by LIF. The measurement accuracy of HO_2 is $\pm 30\%$ (2σ), with an instrument precision of $\pm 2 \times 10^4$ molecules/ cm^3 (typically $\sim 0.5\%$) for 1 min averaged data. Because HO_2 is measured by chemical conversion to OH, the accuracy of the measured $[\text{HO}_2]/[\text{OH}]$ is insensitive to the calibration of the instrument to OH and depends primarily upon the uncertainty in the conversion efficiency of HO_2 to OH within the instrument (approximately $\pm 20\%$).^{7,10} The other molecular species in eq 1 that govern the ratio of $[\text{HO}_2]$ to $[\text{OH}]$ are also measured on the ER-2 flight platform.^{10–16} These are summarized in Table 2 along with pressure and temperature measurements. Rate constants were obtained from DeMore et al.¹⁷ The more recent rate constant evaluation¹⁸ was not utilized because we believe the prior recommendation better represents the laboratory measurements of the rates of the relevant kinetics.¹⁹ All reaction rates were determined using measured concentrations of molecules and atmospheric properties (temperature and air number density). BrO is inferred from the empirical $\text{BrO}-\text{N}_2\text{O}$ relationship²⁰ determined during the ASHOE/MAESA campaign. Because the sampling rate for the ClO measurements is slower than the other measurements, ClO concentrations are interpolated between measurements to a 10 s time average.

Results

The contributions of the individual reaction rate constants and concentrations of eq 1 are shown in Figures 1 and 2. Figure 1 plots altitude versus absolute reaction rate for the ER-2 flight of February 12, 1996, from Barber's Point, HI, consisting of a series of flight legs at different altitudes. The figure shows the transition in chemical reactivity from the stratosphere to the troposphere. The first panel displays the reaction rates governing the conversion of $\text{OH} \rightarrow \text{HO}_2$. The conversion of $\text{OH} \rightarrow \text{HO}_2$ is dominated (almost entirely) by the reaction rate of $\text{OH} + \text{O}_3 \rightarrow \text{HO}_2 + \text{O}_2$ ($r_{\text{OH}+\text{O}_3}$) in the lower stratosphere and by the reaction rate of $\text{OH} + \text{CO} \rightarrow \text{HO}_2 + \text{CO}_2$ ($r_{\text{OH}+\text{CO}}$) in the upper troposphere. The transition between the two reactions occurs at approximately the local tropopause, which is indicated by the dashed line in all three panels.

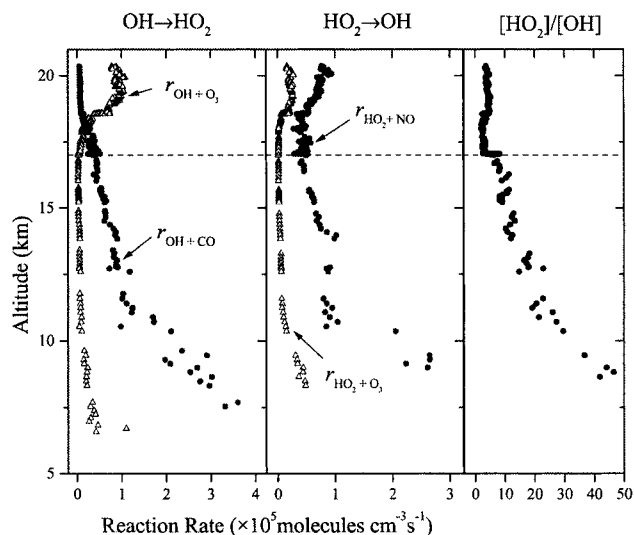


Figure 1. Ten second averaged data from the ER-2 flight of February 12, 1996 out of Barbers Point Naval Air Station, HI. The flight included a number of flight legs at staggered altitudes. (a) Altitude versus reaction rate for reactions important in the conversion of $\text{OH} \rightarrow \text{HO}_2$. The control of $\text{OH} \rightarrow \text{HO}_2$ conversion shifts from the reaction of $\text{OH} + \text{O}_3$ to the reaction of $\text{OH} + \text{CO}$ with decreasing altitude. (b) Altitude versus reaction rate for reactions important in the conversion of $\text{HO}_2 \rightarrow \text{OH}$. Control of conversion in the troposphere depends on the reaction of $\text{HO}_2 + \text{NO}$. (c) Altitude versus $[\text{HO}_2]/[\text{OH}]$. The tropopause for this flight is indicated by the dashed line at ~ 17 km.

The second panel shows the reaction rates governing the conversion of $\text{HO}_2 \rightarrow \text{OH}$. Only the reactions of $\text{HO}_2 + \text{O}_3 \rightarrow \text{OH} + 2\text{O}_2$ and $\text{HO}_2 + \text{NO} \rightarrow \text{OH} + \text{NO}_2$ are shown, because halogen concentrations are insignificant in the lower tropical stratosphere and throughout the upper troposphere. It is apparent from Figure 1 that in the upper troposphere, conversion of $\text{HO}_2 \rightarrow \text{OH}$ depends almost entirely upon the reaction rate of $\text{HO}_2 + \text{NO}$ ($r_{\text{HO}_2+\text{NO}}$). Thus, for the upper troposphere the calculated $[\text{HO}_2]/[\text{OH}]$ reduces to

$$\frac{[\text{HO}_2]}{[\text{OH}]} \approx \frac{k_{\text{OH}+\text{CO}}[\text{CO}]}{k_{\text{HO}_2+\text{NO}}[\text{NO}]} \quad (2)$$

Figure 1 demonstrates the effect of HO_x partitioning on ozone loss and production rates. The increase in $r_{\text{OH}+\text{O}_3}$ and $r_{\text{HO}_2+\text{O}_3}$ above ~ 18 km corresponds to where ozone removal in the lower stratosphere becomes significant. Similarly, $r_{\text{OH}+\text{CO}}$ and $r_{\text{HO}_2+\text{NO}}$ (the rate-limiting step in C3), the rates controlling HO_x partitioning in the upper troposphere, determine the rate of O_3 production in the upper troposphere.^{21,22}

The third panel in Figure 1 displays altitude versus the ratio of $[\text{HO}_2]$ to $[\text{OH}]$. The ratio increases with decreasing altitude in the upper troposphere. Most of this increase can be explained by the increasing concentration of CO and the declining

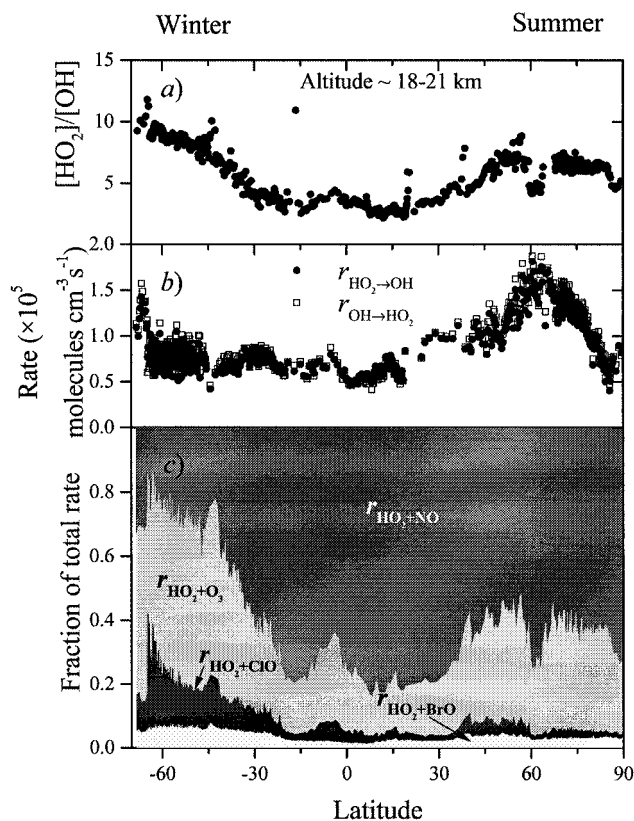


Figure 2. HO_x partitioning as a function of latitude for stratospheric flights during the ASHOE/MAESA and POLARIS NASA ER-2 campaigns. The data are restricted for air densities less than 2.5×10^{18} molecules/cm³, limiting the data to the lower stratosphere, and $[\text{HO}_2] > 8 \times 10^5$ molecules/cm³, removing scatter in the data due to low concentrations of HO_x at high solar zenith angles. Ten second data are sorted by latitude over both ER-2 missions and then averaged into 20 data points per bin. (a) $[\text{HO}_2]/[\text{OH}]$ versus latitude. (b) Total conversion of $\text{OH} \rightarrow \text{HO}_2$ and $\text{HO}_2 \rightarrow \text{OH}$ (circles). The data were not normalized for SZA dependence. (c) Fractional contributions of individual reaction rates to the total conversion of $\text{HO}_2 \rightarrow \text{OH}$. The following nomenclature is used: $r_{\text{HO}_2+\text{NO}}$ refers to the reaction of $\text{HO}_2 + \text{NO} \rightarrow \text{OH} + \text{NO}_2$, $r_{\text{HO}_2+\text{O}_3}$ refers to $\text{HO}_2 + \text{O}_3 \rightarrow \text{OH} + 2\text{O}_2$, $r_{\text{HO}_2+\text{ClO}}$ refers to $\text{HO}_2 + \text{ClO} \rightarrow \text{HOCl} + \text{O}_2$, and $r_{\text{HO}_2+\text{BrO}}$ refers to $\text{HO}_2 + \text{BrO} \rightarrow \text{HOBr} + \text{O}_2$.

concentration of NO at lower altitudes. The abrupt change in $[\text{HO}_2]/[\text{OH}]$ at the tropopause reflects the change in the mechanism for conversion of $\text{OH} \rightarrow \text{HO}_2$ from the reaction of $\text{OH} + \text{O}_3$ in the lower stratosphere to the reaction of $\text{OH} + \text{CO}$ in the upper troposphere.

Figure 2 shows HO_x partitioning from the ER-2 flight platform as a function of latitude from 70°S to 90°N. The data set was obtained from ASHOE/MAESA and POLARIS. STRAT data were not utilized because ClO was not measured during STRAT. Ascents and descents from Fairbanks, AL, during POLARIS have been excluded from the data. The data are restricted to air number densities (M) less than 2.5×10^{18} molecules/cm³, limiting the data to the stratosphere. Ten second data were sorted by latitude and then averaged into 20 data points per bin. The top panel (a) displays $[\text{HO}_2]/[\text{OH}]$ versus latitude, the middle panel (b) the rates for the total conversion of $\text{OH} \rightarrow \text{HO}_2$ and $\text{HO}_2 \rightarrow \text{OH}$, and the bottom panel (c) the fractional contributions of the individual reaction rates to the total conversion of $\text{HO}_2 \rightarrow \text{OH}$. Only individual reactions for $\text{HO}_2 \rightarrow \text{OH}$ conversion are plotted because the only significant $\text{OH} \rightarrow \text{HO}_2$ conversion process in the lower/middle stratosphere in this data set is the reaction of $\text{OH} + \text{O}_3$ (Figure 1).

The latitudinal variations in Figure 2 are dominated by the fractional contributions of $r_{\text{HO}_2+\text{NO}}$ and $r_{\text{HO}_2+\text{O}_3}$. In Figure 2c, the boundary between $r_{\text{HO}_2+\text{NO}}$ and $r_{\text{HO}_2+\text{O}_3}$ represents the fraction of HO_x cycling that results in O_3 loss. Above the boundary, $r_{\text{HO}_2+\text{NO}}$ represents a null cycle regarding O_3 loss. Below the boundary, the individual rates $r_{\text{HO}_2+\text{BrO}}$, $r_{\text{HO}_2+\text{ClO}}$, and $r_{\text{HO}_2+\text{O}_3}$ are the rate-limiting steps for ozone removal by HO_x cycling in the lower stratosphere. The fractional contribution of $r_{\text{HO}_2+\text{BrO}}$ to the conversion of $\text{HO}_2 \rightarrow \text{OH}$ is small over the whole latitude space. The fractional contribution of $r_{\text{HO}_2+\text{ClO}}$ to the conversion of $\text{HO}_2 \rightarrow \text{OH}$ is only important when the conversion of total inorganic chlorine ($\text{Cl}_y = \text{HCl} + \text{ClONO}_2 + \text{HOCl} + \text{ClO} + \text{Cl}$) to highly reactive chlorine radicals ($\text{Cl}_x = \text{Cl} + \text{ClO}$) that effectively destroy O_3 becomes large near the polar winter vortex.

The results in Figure 2 reveal a sampling bias from both ASHOE/MAESA and POLARIS. The fractional contribution of O_3 plotted in Figure 2c reflects latitudinal changes in the height of the local tropopause. The tropopause is at a higher altitude in the tropics (~ 17 km in Figure 1) and decreases in altitude with increasing latitude, becoming less defined in the polar regions (~ 9 – 10 km). Because the ER-2 flies at roughly a constant cruise altitude (~ 20 km) in the lower stratosphere, the ER-2 samples higher in the stratosphere in mid and high latitudes and lower in the stratosphere in the tropics. The decrease in the absolute reaction rate of $\text{HO}_2 + \text{O}_3$ in the tropics represents the decrease in the $[\text{O}_3]$ near the tropical tropopause. $[\text{HO}_2]/[\text{OH}]$ in the top panel mirrors these fractional changes in O_3 concentration with latitude.

The high-latitude data shows the effects of changes in the partitioning of the nitrogen and chlorine families. In the lower stratosphere, the N_2O_5 hydrolysis reaction on aerosols ($\text{N}_2\text{O}_5 + \text{H}_2\text{O} \xrightarrow{\text{SA}} 2\text{HNO}_3$) is an important sink for NO_x ($\text{NO} + \text{NO}_2$).^{23,24} This conversion (dependent on the formation of N_2O_5 , which occurs primarily at night) competes with the gas-phase conversion of HNO_3 to NO_2 by photolysis and reaction with OH . Seasonal changes in the relative heterogeneous and gas-phase conversion rates drive changes in NO_x concentrations. The smaller fractional contribution of $r_{\text{HO}_2+\text{NO}}$ at high southern latitudes reflects the dominance of the heterogeneous process over gas-phase processes that result in the conversion of NO_x to NO_y (total odd nitrogen species). In contrast, data obtained at 60–90°N during the arctic polar summer show enhanced NO_x concentrations. During the conditions of nearly continuous solar illumination experienced during POLARIS, photolysis of NO_3 reduces the formation of N_2O_5 , decreasing HNO_3 formation and driving the NO_y reservoir into NO_x .

In the absence of polar processing, ClO and NO_x concentrations are strongly coupled through the formation of ClONO_2 .²⁵ The observed fractional contributions of $r_{\text{HO}_2+\text{NO}}$ and $r_{\text{HO}_2+\text{ClO}}$ are inversely correlated. The data obtained near 70°S latitude during polar winter show relatively high halogen and low NO_x concentrations typical at the edge of the polar vortex. During the conditions of nearly continuous solar illumination, high levels of NO_x drive ClO into ClONO_2 , resulting in the low ClO concentrations observed during the polar summer.

The high $[\text{NO}_x]$ observed during polar summer results in increased cycling of HO_x . This is observed in Figure 2b by the increased reaction rates for the total $\text{HO}_2 \rightarrow \text{OH}$ conversion and $\text{OH} \rightarrow \text{HO}_2$ conversion at high northern latitudes. While Figure 2b shows the rate of HO_x cycling, it gives no information about the efficiency of O_3 loss due to HO_x cycling. The efficiency of ozone loss depends on the relative importance of each process in the conversion of $\text{HO}_2 \rightarrow \text{OH}$. When $r_{\text{HO}_2+\text{NO}}$

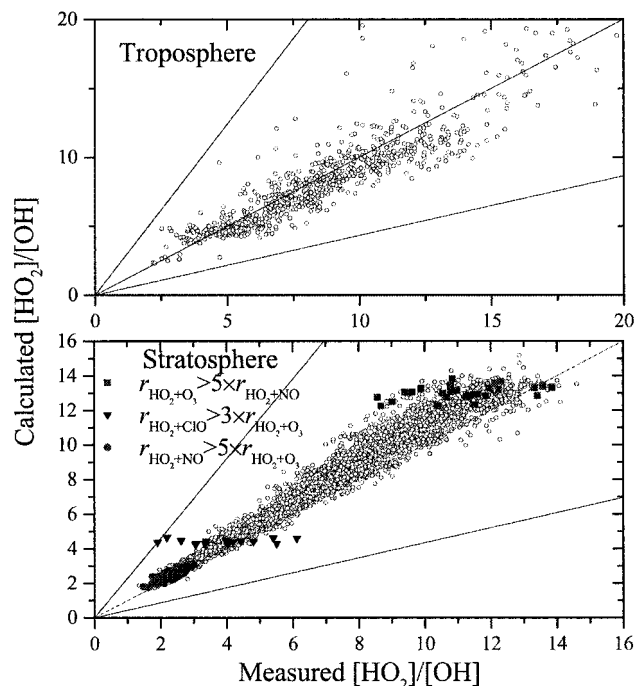


Figure 3. Calculated versus measured $[\text{HO}_2]/[\text{OH}]$ in the upper troposphere (a) and lower stratosphere (b). Both tropospheric and stratospheric data sets are averaged over a 1 min time interval. The tropospheric data set was obtained from the STRAT mission. Tropospheric data were restricted so that $r_{\text{OH}+\text{CO}} > 8 \times r_{\text{OH}+\text{O}_3}$, ensuring that the data points are from the upper troposphere. Data were also restricted so that $r_{\text{HO}_2+\text{NO}} > 8 \times r_{\text{HO}_2+\text{OH}}$, the primary loss mechanism for HO_x . Stratospheric data points were restricted as in Figure 2. The dashed lines in both a and b are the calculated ratios determined by adjusting the rate constants for the relevant terms to their 1σ uncertainty limits at 215 K and then adding the errors in quadrature. The solid data points shown in Figure 3b represent where the conversion of $\text{HO}_2 \rightarrow \text{OH}$ is dominated by $r_{\text{HO}_2+\text{NO}}$ (circles), $r_{\text{HO}_2+\text{ClO}}$ (triangles), and $r_{\text{HO}_2+\text{O}_3}$ (squares). Data for these regions are averaged into 10 s bins. Further selection criteria for these data are discussed in the text and below for Figure 4.

controls the conversion of $\text{HO}_2 \rightarrow \text{OH}$, the efficiency for ozone loss is low because $r_{\text{HO}_2+\text{NO}}$ represents the null cycle regarding ozone loss. In contrast, when $r_{\text{HO}_2+\text{O}_3}$ controls the conversion of $\text{HO}_2 \rightarrow \text{OH}$, the efficiency for ozone loss is high.

The middle panel in Figure 2 also shows that the conversion of $\text{OH} \rightarrow \text{HO}_2$ is approximately equivalent to the total conversion of $\text{HO}_2 \rightarrow \text{OH}$. It is important to note that OH and HO_2 are not constrained to be equivalent in Figure 2b. The agreement between $\text{OH} \rightarrow \text{HO}_2$ and $\text{HO}_2 \rightarrow \text{OH}$ is an indication of how well the system is described and shows that the steady-state approximation holds. While individual reaction rates vary in magnitude with latitude, the total conversion of $\text{HO}_2 \rightarrow \text{OH}$ is relatively flat, only showing an increase during POLARIS at high northern latitudes during summer when NO concentrations are high.

Figure 3 shows the comparison between the calculated and measured $[\text{HO}_2]/[\text{OH}]$ ratio in the upper troposphere (a) and lower stratosphere (b). Tropospheric and stratospheric data sets are averaged over a 1 min time interval. The tropospheric data set was obtained from the STRAT mission. Tropospheric data were restricted so that $r_{\text{OH}+\text{CO}} > 8 \times r_{\text{OH}+\text{O}_3}$. This ensures that the data points are located in the upper troposphere. Data were also restricted so that $r_{\text{HO}_2+\text{NO}} > 8 \times r_{\text{HO}_2+\text{OH}}$, the primary loss mechanism for HO_x . This condition ensures that HO_x cycling is much faster than HO_x production or loss in the upper troposphere. Using this selection criteria retains $\sim 90\%$ of the available data in the region from 10 km to the tropopause. The

stratospheric data set was obtained from the ASHOE/MAESA and POLARIS missions. Stratospheric data were restricted to $M < 2.5 \times 10^{18}$ molecules/cm³ and solar zenith angles less than 85° . Shown as dashed lines in Figure 3 in both parts a and b are the calculated ratios determined by adjusting the rate constants for all the relevant terms to their 1σ uncertainty limits at 215 K and then calculating the weighted root sum of the squares on the uncertainties. For the tropospheric data in Figure 3a, $\sim 83\%$ of the uncertainty in the 1σ limits is due to uncertainty in $k_{\text{OH}+\text{CO}}$. For the stratospheric data $\sim 80\%$ of the uncertainty in the 1σ limits is due to the uncertainty in $k_{\text{OH}+\text{O}_3}$.

The agreement between the calculated and measured ratios, in both the upper troposphere and lower stratosphere, is remarkable given the vast size of the data set. The mean value of the calculated ratio divided by the measured ratio is 0.97 ± 0.17 in the upper troposphere and 1.11 ± 0.07 in the lower stratosphere over a wide range of latitude, altitude, and season. As discussed previously by Cohen et al.,⁷ the agreement between the measured and calculated $[\text{HO}_2]/[\text{OH}]$ ratios is much better than indicated by 1σ uncertainties in either the instruments or the reported reaction rates. Data in the upper troposphere shows more scatter than in the lower stratosphere, primarily because of decreased precision in the observed mixing ratios of HO_2 and OH in the upper troposphere. The decreased precision results from low mixing ratios of OH and HO_2 and increased background noise in the measurement of HO_x at lower altitude.

The small ($\sim 10\%$) disagreement between the calculated and measured ratio in the lower stratosphere suggests one or more of the following: our understanding of HO_x partitioning is incomplete, there is an unexplained error in one or more of the measurements, or at least one of the rate constants is incorrect. The chemistry that controls HO_x partitioning is extremely fast. While missing chemistry from eq 1 cannot be excluded, it is unlikely because it would have to compete on the same time scale as the reactions in Table 1. An error in the HO_x measurement is possible; however, it would have to be offset by either pressure or a corresponding error in one of the two measurements or rate constants that control the HO_x partitioning in the upper troposphere. The accuracy of measuring $[\text{HO}_2]/[\text{OH}]$ should not change with altitude—the measurement uncertainties take into account variations in temperature and pressure. Regressions of the calculated to the measured $[\text{HO}_2]/[\text{OH}]$ versus each of the different measurements does not show any correlation that would account for the 10% shift. However, the dynamic range of some of the measurements is small, so relationships between certain variables may not be obvious in the correlation plots. Other $[\text{HO}_2]/[\text{OH}]$ studies²⁶ during the NASA SONEX (SASS Ozone and Nitrogen Oxide Experiment) DC-8 aircraft campaign show agreement between the calculated ratio and the measured ratio with a mean value of 1.05 ± 0.30 . Separate analyses of $[\text{NO}]/[\text{NO}_2]$ show that the NO and O_3 measurements used in these calculations are consistent with two independent measurements of NO_2 and the appropriate rate constants.^{27,28}

Uncertainties in the laboratory rate constant data can also influence the observed offset. Regressions of the calculated-to-measured ratio versus each of the rate constants in ref 17 does not show any obvious correlation. This does not mean that errors in those rate constants cannot exist; covariance between variables (for example, O_3 and temperature) can influence the regression plots. Recent measurements of $k_{\text{HO}_2+\text{O}_3}$ indicate that this rate constant may be slightly greater than the value given by DeMore et al.¹⁷ at low temperatures.²⁹ This result shifts the stratospheric data $\sim 5\%$ closer to the 1:1 line while having essentially no effect on the tropospheric data. Additionally, recent work by

Nizkorodov et al.³⁰ measures the sum of $k_{\text{OH}+\text{O}_3}$ and $k_{\text{HO}_2+\text{O}_3}$ over the temperature range 190–315 K. The $k_{\text{OH}+\text{O}_3}$ derived by subtracting $k_{\text{HO}_2+\text{O}_3}$ from the sum of the rates determined in this study shifts the stratospheric data away from the 1:1 line, increasing the discrepancy between the modeled-to-measured ratio by ~ 10 –15%, depending upon the value used for $k_{\text{HO}_2+\text{O}_3}$. These low-temperature studies by Herndon et al.²⁹ and Nizkorodov et al.³⁰ are not included in the recent reevaluation of the Jet Propulsion Laboratory's rate constants.¹⁸ It is likely that a single factor is not responsible for the disagreement between the measured and modeled $[\text{HO}_2]/[\text{OH}]$ and that a number of small errors from multiple terms cause this discrepancy.

The solid data points shown in Figure 3b represent regions of the lower stratosphere where the conversion of $\text{HO}_2 \rightarrow \text{OH}$ is governed by (a) $r_{\text{HO}_2+\text{NO}}$ (C3), (b) $r_{\text{HO}_2+\text{ClO}}$ (C2), and (c) $r_{\text{HO}_2+\text{O}_3}$ (C1). Data for these regions were restricted by atmospheric number density and SZA, as in the larger stratospheric data set. Additional restriction criteria were (1) $r_{\text{OH}+\text{O}_3} > 5 \times r_{\text{OH}+\text{CO}}$ as a further check that all data points came from the lower stratosphere, (2) $[\text{OH}] > 2 \times 10^5$ molecules/cm³ and $[\text{HO}_2] > 8 \times 10^5$ molecules/cm³ were used to remove scatter in the data due to low concentrations of HO_x at higher solar zenith angles, and (3) the dominant reaction for $\text{HO}_2 \rightarrow \text{OH}$ conversion was required to be a factor of 5 greater than competing reactions. For example, the selection criteria for the data dominated by $r_{\text{HO}_2+\text{NO}}$ is $r_{\text{HO}_2+\text{NO}} > 5 \times r_{\text{HO}_2+\text{O}_3}$ and $r_{\text{HO}_2+\text{NO}} > 5 \times r_{\text{HO}_2+\text{ClO}}$. All data were averaged to 10 s.

These same three data regions in the lower stratosphere are plotted versus temperature in Figure 4. Figure 4a illustrates how well the effects of individual reactions on the ratio of $[\text{HO}_2]$ to $[\text{OH}]$ can be isolated. The measured data points are represented by open symbols, modeled data points by black dots. The lines through each of the data regions are model curves generated using the median value of each chemical species as an input parameter. The different slopes seen for each of the model curves represent the effect of a change in temperature on the different reactions that govern the HO_x ratio in that region. The error bars shown in the plot represent the uncertainty in the precision of the HO_x measurements.

When $r_{\text{HO}_2+\text{ClO}}$ governs the conversion of $\text{HO}_2 \rightarrow \text{OH}$ in the lower stratosphere and HOCl is in steady state (the reaction rate of $\text{HO}_2 + \text{ClO} \rightarrow \text{HOCl} + \text{O}_2 \equiv$ the reaction rate of $\text{HOCl} + h\nu \rightarrow \text{OH} + \text{Cl}$), eq 1 is reduced to

$$\frac{[\text{HO}_2]}{[\text{OH}]} \approx \frac{k_{\text{OH}+\text{O}_3}[\text{O}_3] + k_{\text{OH}+\text{ClO}}[\text{ClO}]}{k_{\text{HO}_2+\text{ClO}}[\text{ClO}]} \quad (3)$$

The data set is very limited for this condition. Due to a sparse data set, the selection requirements for $r_{\text{HO}_2+\text{ClO}}$ were relaxed to $[\text{OH}] > 1 \times 10^5$ molecules/cm³, $[\text{HO}_2] > 1 \times 10^5$ molecules/cm³, and $r_{\text{HO}_2+\text{ClO}} > 3 \times r_{\text{HO}_2+\text{O}_3}$. Even with relaxing the selection criteria, the number of data points still remains small and the scatter in the data is large. All of the data points where $r_{\text{HO}_2+\text{ClO}}$ controls the $\text{HO}_2 \rightarrow \text{OH}$ conversion come from two flights during ASHOE/MAESA; on July 28 and July 30, 1994.

When $r_{\text{HO}_2+\text{O}_3}$ controls the conversion of $\text{HO}_2 \rightarrow \text{OH}$ in the lower stratosphere, eq 1 is reduced to only the terms present in the HO_x -catalyzed ozone removal cycle (C1):

$$\frac{[\text{HO}_2]}{[\text{OH}]} \approx \frac{k_{\text{OH}+\text{O}_3}[\text{O}_3]}{k_{\text{HO}_2+\text{O}_3}[\text{O}_3]} \quad (4)$$

This data set is also limited, indicating there is only a small portion of the sampled atmosphere where HO_x partitioning

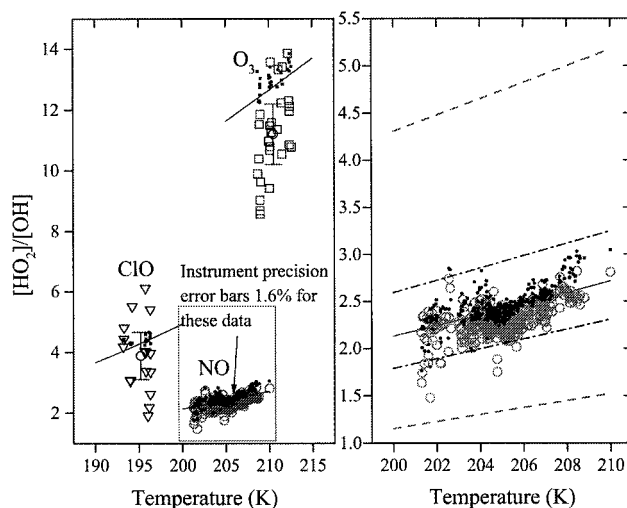


Figure 4. (a) $[\text{HO}_2]/[\text{OH}]$ is shown versus temperature for the limiting cases where the conversion of $\text{HO}_2 \rightarrow \text{OH}$ is governed by $[\text{ClO}]$ (open triangles), $[\text{O}_3]$ (open squares), and $[\text{NO}]$ (open circles). Measured data points are represented by open symbols, modeled data points by black dots. The solid lines through each of the data regions are model curves generated using the median value of each chemical species as an input parameter with only temperature as a variable. The error bars shown in the plot represent the uncertainty in the precision of the HO_x instrument (instrument precision was calculated by dividing the standard deviation in the OH and HO_2 signals by the mean observed signal in OH and HO_2 and then adding the errors in quadrature). The limiting cases are determined by restricting each subset according to the following criteria. For ClO , $r_{\text{HO}_2+\text{ClO}} > 3 \times r_{\text{HO}_2+\text{O}_3}$ and $r_{\text{HO}_2+\text{ClO}} > 5 \times r_{\text{HO}_2+\text{NO}}$; for O_3 , $r_{\text{HO}_2+\text{O}_3} > 5 \times r_{\text{HO}_2+\text{NO}}$ and $r_{\text{HO}_2+\text{O}_3} > 5 \times r_{\text{HO}_2+\text{ClO}}$; and for NO , $r_{\text{HO}_2+\text{NO}} > 5 \times r_{\text{HO}_2+\text{O}_3}$ and $r_{\text{HO}_2+\text{NO}} > 5 \times r_{\text{HO}_2+\text{ClO}}$. (b) Expanded view of $[\text{HO}_2]/[\text{OH}]$ versus temperature for the limiting cases where the conversion of $\text{HO}_2 \rightarrow \text{OH}$ is governed by NO . The dashed dot black lines in 4b correspond to $k_{\text{HO}_2+\text{NO}}$ being adjusted to its 1σ uncertainty limits for the modeled ratio generated using the median value of each chemical species as an input parameter from 200 to 210K. The dashed lines in 4b correspond to $k_{\text{OH}+\text{O}_3}$ being adjusted to its 1σ uncertainty limits for the modeled ratio generated using the median value of each chemical species as an input parameter from 200 to 210K.

depends primarily upon O_3 . The data for $r_{\text{HO}_2+\text{O}_3}$, while having more points and less scatter than that for $r_{\text{HO}_2+\text{ClO}}$, were obtained from only one flight during ASHOE/MAESA, on June 3, 1994.

The discrepancy between the measured and the modeled values for $r_{\text{HO}_2+\text{ClO}}$ or $r_{\text{HO}_2+\text{O}_3}$ is due, in part, to instrument limitations at high solar zenith angles. Instrument precision plays a large role in the measurement uncertainties when HO_x concentrations approach the detection limits. For the limiting case where $r_{\text{HO}_2+\text{ClO}}$ dominates conversion of $\text{HO}_2 \rightarrow \text{OH}$, the uncertainty in the instrument precision is large because both $[\text{HO}_2]$ and $[\text{OH}]$ are small. The instrument precision for this subset of data was calculated to be 21%. These data were obtained in the winter polar regions where SZAs are large ($\sim 80^\circ$). For the limiting case where $r_{\text{HO}_2+\text{O}_3}$ dominates conversion of $\text{HO}_2 \rightarrow \text{OH}$, the uncertainty in the instrument precision is large because the $[\text{OH}]$ is low. The instrument precision when $r_{\text{HO}_2+\text{O}_3}$ governs $\text{HO}_2 \rightarrow \text{OH}$ conversion was calculated to be 9.6%.

When $r_{\text{HO}_2+\text{NO}}$ dominates the conversion of $\text{HO}_2 \rightarrow \text{OH}$ in the lower stratosphere, eq 1 reduces to

$$\frac{[\text{HO}_2]}{[\text{OH}]} \approx \frac{k_{\text{OH}+\text{O}_3}[\text{O}_3]}{k_{\text{HO}_2+\text{NO}}[\text{NO}]} \quad (5)$$

The data for this limiting case are tightly grouped at low values of $[\text{HO}_2]/[\text{OH}]$ in Figure 4a. These data points come from

multiple flights from both ASHOE/MAESA and POLARIS. The large number of points in this grouping is consistent with $\text{HO}_2 + \text{NO}$ being the primary reaction for the conversion of $\text{HO}_2 \rightarrow \text{OH}$ over a broad latitude range (see Figure 2). For this limiting case in the conversion of $\text{HO}_2 \rightarrow \text{OH}$, the uncertainty in the instrument precision is negligible ($\sim 1.6\%$) because both $[\text{HO}_2]$ and $[\text{OH}]$ are relatively large. In addition, over the temperature range 200–210K $[\text{O}_3]/[\text{NO}]$ varies by only $\sim 10\%$, indicating that the concentrations of $[\text{O}_3]$ and $[\text{NO}]$ are relatively independent of temperature using the selection criteria in Figure 4. Because $[\text{O}_3]$ and $[\text{NO}]$ are relatively independent of temperature, and due to the high instrument precision, the effect of a change in temperature can be seen directly in the observed $[\text{HO}_2]/[\text{OH}]$.

Figure 4b shows an expanded view of $[\text{HO}_2]/[\text{OH}]$ versus temperature for the limiting case where the conversion of $\text{HO}_2 \rightarrow \text{OH}$ is governed by $[\text{NO}]$ (eq 5 above). The dashed dot black lines correspond to $k_{\text{HO}_2 + \text{NO}}$ being adjusted to its 1σ uncertainty limits for the modeled ratio and the dashed lines correspond to $k_{\text{OH} + \text{O}_3}$ being adjusted to its 1σ uncertainty limits for the modeled ratio. Both uncertainties were generated using the median value of each chemical species as an input parameter from 200 to 210K. For a constant value of NO and O_3 , Figure 4b is how HO_x responds to a change in temperature. The Arrhenius expression ($Ae^{-E/RT}$) for $k_{\text{HO}_2 + \text{NO}}$ has an activation energy $-(E/R \pm \Delta E/R)/T$ of $(250 \pm 50)/T$, while the expression for $k_{\text{OH} + \text{O}_3}$ has an activation energy of $-(940 \pm 300)/T$.¹⁷ The majority of the temperature dependence observed in the slope in Figure 4b is due to $k_{\text{OH} + \text{O}_3}$. The activation energy for eq 5 using data from ref 17 is $-(E/R \pm \Delta E/R)/T = -(1190 \pm 304)/T$. The fit to the calculated data (solid line) gives $-(E/R \pm \Delta E/R)/T = -(1242 \pm 65)/T$; the fit to the measured values gives $-(E/R \pm \Delta E/R)/T = -(1045 \pm 81)/T$. The activation energies are all reasonably close. The difference between the Jet Propulsion Laboratory's recommendation and the calculated fit shows that our selection criteria are not exact. The difference between the measured fit and calculated fit may be due to an error in one or more of the rate constants or due to our use of a small data set over a limited temperature range.

The response of $[\text{HO}_x]$ to a perturbation of $[\text{ClO}]$ and $[\text{BrO}]$ is not well-determined because of the limited dynamic range in the data set for halogen species. However, the data set for showing the response of $[\text{HO}_x]$ to $[\text{NO}_x]$ is very good. Figure 5 shows the measured and modeled $[\text{HO}_2]/[\text{OH}]$ versus $[\text{NO}_x]$ for different levels of ozone in the lower stratosphere. While the variation in $[\text{HO}_2]$ is driven by $[\text{NO}]$, the concentration of NO as a function of $[\text{NO}_x]$ varies proportionally to $[\text{O}_3]$, allowing Figure 5 to be made. $[\text{NO}_2]$ was determined from a steady-state relation because $[\text{NO}_2]$ measurements were not available for a large number of flights in the data set. The difference between the $[\text{NO}_2]$ steady-state value and measured value is less than 10%.²⁸ Data were restricted for a given value of $[\text{O}_3]$ with $\text{SZA} < 77^\circ$ and for low halogen concentrations. The difference between the modeled curves and the measured points shows the 10% error observed in Figure 3.

Because the concentration of OH is a simple function of SZA in the lower stratosphere, OH concentrations do not vary with $[\text{NO}_x]$ and $[\text{O}_3]$.¹ In contrast, HO_2 concentrations do vary with the concentration of other chemical species. Plotting $[\text{HO}_2]/[\text{OH}]$ reflects these variations in $[\text{HO}_2]$ and effectively removes any SZA dependence. Thus, the response of catalytically active $[\text{HO}_2]$ to changes in $[\text{NO}_x]$ and $[\text{O}_3]$ is observed directly in Figure 5, and $[\text{HO}_2]/[\text{OH}]$ represents how $[\text{HO}_x]$ responds to variations in $[\text{NO}_x]$ and $[\text{O}_3]$ in the lower stratosphere. For a

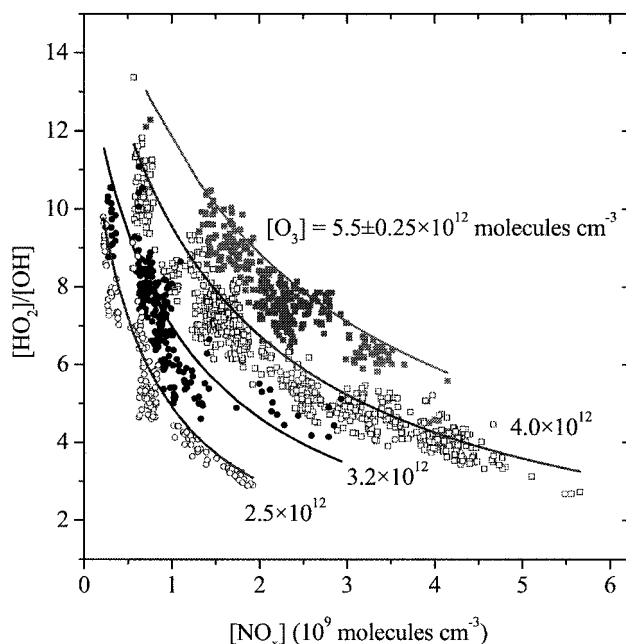


Figure 5. Measured and modeled HO_2/OH concentrations versus $[\text{NO}_x]$ ($[\text{NO}] + [\text{NO}_2]$) for different levels of ozone in the lower stratosphere. Data were restricted for $\text{SZA} < 77^\circ$ and low halogen levels ($[\text{ClO}] < 1 \times 10^8$ molecules/ cm^3). The model curves are generated from eq 1 using the median values for temperature and of each chemical species as input parameters. $[\text{NO}_x]$ was obtained from NO measurements and a steady-state calculation for $[\text{NO}_2]$: $([\text{NO}_2] = (k_{\text{NO} + \text{O}_3}[\text{O}_3] + k_{\text{NO} + \text{ClO}}[\text{ClO}][\text{NO}] \div J_{\text{NO}_2})$. The range of O_3 values allowed for the observations of each median O_3 value is 0.25×10^{12} molecules cm^{-3} .

given value of $[\text{NO}_x]$, HO_x concentrations are directly proportional to $[\text{O}_3]$. At low ozone concentrations, where $r_{\text{HO}_2 + \text{NO}}$ dominates the conversion of $\text{HO}_2 \rightarrow \text{OH}$, $[\text{HO}_x]$ is extremely sensitive to changes in $[\text{NO}_x]$. In the limiting case where $r_{\text{HO}_2 + \text{NO}}$ dominates the conversion of $\text{HO}_2 \rightarrow \text{OH}$ (eq 5), the concentration of HO_x is inversely proportional to the concentration of NO_x . Thus, the rate-limiting steps in cycles 1 and 2 are an inverse function of $[\text{NO}_x]$.

Summary and Conclusions

We have shown that HO_x partitioning is accurately described in the lower stratosphere and upper troposphere (~ 10 km to tropopause) by $[\text{HO}_2]/[\text{OH}]$ expressed in eq 1, with the modeled ratio overpredicting the measured ratio by 10% in the lower stratosphere. This is true over changes in altitude, latitude, and season. This ratio includes the rate-limiting steps for removal of O_3 by HO_x in the lower stratosphere and production of O_3 in the upper troposphere. As exhibited in Figure 2, the dominant HO_x cycling reaction throughout most of the lower stratosphere results in a null cycle regarding ozone loss. Comparison of the measured to modeled HO_x ratio shows that the in situ measurements of OH, HO_2 , NO, CO, O_3 , ClO, and BrO as well as the corresponding rate constants are consistent over a wide range of atmospheric conditions.

The effects of temperature dependence on the regions of the lower stratosphere where the conversion of $\text{HO}_2 \rightarrow \text{OH}$ is governed by predominantly one reaction have been examined. When $r_{\text{HO}_2 + \text{ClO}}$ dominates $\text{HO}_2 \rightarrow \text{OH}$ conversion, the data set is sparse and exhibits scatter too great to obtain any relevant information. The role of BrO has yet to be quantitatively examined. SOLVE (SAGE III Ozone Loss Validation Experiment), the ER-2 field campaign completed during the winter of 2000, will be crucial in mapping out this reaction space of

the lower stratosphere. For the limiting case where O_3 concentrations govern $[HO_2]/[OH]$ (eq 4), the agreement between the calculated and measured ratio is poor, because there is a limited portion of the sampled atmosphere where the ratio depends solely on $[O_3]$ (see Figure 2). Agreement of measured to modeled $[HO_2]/[OH]$ for the limiting case where r_{HO_2+NO} governs $HO_2 \rightarrow OH$ conversion shows how well k_{HO_2+NO} and NO concentrations are known. This is the only case for the lower stratosphere where there is sufficient data to examine how a change in temperature affects the ratio of HO_2 to OH .

While HO_x partitioning is, we believe, well-understood by the measurements and rate constants in eq 1, the success of the $[HO_2]/[OH]$ analysis to determine catalytic ozone loss through C1 and C2 is mixed. $[OH]$ depends primarily on SZA in the lower stratosphere, while $[HO_2]/[OH]$ reflects the coupling of $[HO_2]$ to the concentrations of other chemical species. Therefore, the response of $[HO_2]/[OH]$ is representative of how HO_x concentrations respond to photochemical variations in the lower stratosphere. At low halogen levels, Figure 5 demonstrates that the response of $[HO_x]$ is established for changes in $[NO_x]$ and $[O_3]$ to ~ 10 –20%. For the existing data, $[HO_2]/[OH]$ is inversely proportional to $[NO_x]$ and directly proportional to $[O_3]$. Further measurements are necessary in order to fully illustrate the response of $[HO_x]$ to changes in halogen concentrations. Figure 5 also reflects the branching among cycles 1 to 3 (for low halogen) and shows the efficiency of O_3 removal by HO_x cycling. When $[NO_x]$ is high, O_3 removal by HO_x is inefficient. When $[NO_x]$ is low, O_3 removal by HO_x is more efficient. Regardless of the branching among C1 to C3, the key step for all of these HO_x partitioning cycles is the initiation reaction of $OH+O_3$.

Acknowledgment. We thank the pilots and crew of the NASA ER-2. Thank you to C. R. Webster, R. D. May, and R. Herman for use of the ALIAS-CO measurements in this analysis and D. W. Fahey for use of the NO measurements. The ASHOE/MAESA, STRAT, and POLARIS ER-2 programs were supported by NASA through the Upper Atmosphere Research Program, the Atmospheric Effects of Aviation Project, and the Atmospheric Chemistry Modeling and Analysis Program.

References and Notes

- Hanisco, T. F.; Lanzendorf, E. J.; Wennberg, P. O.; Perkins, K. K.; Stimpfle, R. M.; Voss, P. B.; Anderson, J. G.; Cohen, R. C.; Fahey, D. W.; Gao, R. S.; Hints, E. J.; Salawitch, R. J.; Margitan, J. J.; McElroy, T.; Midwinter, C. *J. Phys. Chem. A* **2001**, *105*, 1543.
- Logan, J. A.; Prather, M. A.; Wofsy, S. C.; McElroy, M. B. *J. Geophys. Res.—Atmos.* **1981**, *86*, 7210.
- Wennberg, P. O.; Cohen, R. C.; Stimpfle, R. M.; Koplow, J. P.; Anderson, J. G.; Salawitch, R. J.; Fahey, D. W.; Woodbridge, E. L.; Keim, E. R.; Gao, R. S.; Webster, C. R.; May, R. D.; Toohey, D. W.; Avallone, L. M.; Proffitt, M. H.; Loewenstein, M.; Podolske, J. R.; Chan, K. R.; Wofsy, S. C. *Science* **1994**, *266*, 398.
- Davis, D. D.; Crawford, J.; Chen, G.; Chameides, W.; Liu, S.; Bradshaw, J.; Sandholm, S.; Sachse, G.; Gregory, G.; Anderson, B.; Barrick, J.; Bachmeier, A.; Collins, J.; Brown, E.; Blake, D.; Rowland, S.; Kondo, Y.; Singh, H.; Talbot, R.; Heikes, B.; Merrill, J.; Rodriguez, J.; Newell, R. E. *J. Geophys. Res.—Atmos.* **1996**, *101*, 2111.
- Jucks, K. W.; Johnson, D. G.; Chance, K. V.; Traub, W. A.; Margitan, J. J.; Osterman, G. B.; Salawitch, R. J.; Sasano, Y. *Geophys. Res. Lett.* **1998**, *25*, 3935.
- Brune, W. H.; Faloona, I. C.; Tan, D.; Weinheimer, A. J.; Campos, T.; Ridley, B. A.; Vay, S. A.; Collins, J. E.; Sachse, G. W.; Jaegle, L.; Jacob, D. J. *Geophys. Res. Lett.* **1998**, *25*, 1701.
- Cohen, R. C.; Wennberg, P. O.; Stimpfle, R. M.; Koplow, J.; Anderson, J. G.; Fahey, D. W.; Woodbridge, E. L.; Keim, E. R.; Gao, R.; Proffitt, M. H.; Loewenstein, M.; Chan, K. R. *Geophys. Res. Lett.* **1994**, *21*, 2539.
- Wennberg, P. O.; Stimpfle, R. M.; Weinstock, E. M.; Dessler, A. E.; Lloyd, S. A.; Lapson, L. B.; Schwab, J. J.; Anderson, J. G. *Geophys. Res. Lett.* **1990**, *17*, 1909.
- Johnston, H. S.; Podolske, J. R. *Rev. Geophys. Space Phys.* **1978**, *6*, 491.
- Wennberg, P. O.; Cohen, R. C.; Hazen, N. L.; Lapson, L. B.; Allen, N. T.; Hanisco, T. F.; Oliver, J. F.; Lanham, N. W.; Demusz, J. N.; Anderson, J. G. *Rev. Sci. Instrum.* **1994**, *65*, 1858.
- Proffitt, M. H.; Steinkamp, M. J.; Powell, J. A.; McLaughlin, R. J.; Mills, O. A.; Schmeltekopf, A. L.; Thompson, T. L.; Tuck, A. F.; Tyler, T.; Winkler, R. H.; Chan, K. R. *J. Geophys. Res.—Atmos.* **1989**, *94*, 16547.
- Fahey, D. W.; Kelly, K. K.; Ferry, G. V.; Poole, L. R.; Wilson, J. C.; Murphy, D. M.; Loewenstein, M.; Chan, K. R. *J. Geophys. Res.—Atmos.* **1989**, *94*, 11299.
- Webster, C. R.; May, R. D.; Trimble, C. A.; Chave, R. G.; Kendall, J. *Appl. Optics* **1994**, *33*, 454.
- Brune, W. H.; Anderson, J. G.; Chan, K. R. *J. Geophys. Res.—Atmos.* **1989**, *94*, 16639.
- Brune, W. H.; Anderson, J. G.; Chan, K. R. *J. Geophys. Res.—Atmos.* **1989**, *94*, 16649.
- Chan, K. R.; Scott, S. G.; Bui, T. P.; Bowen, S. W.; Day, J. J. *J. Geophys. Res.—Atmos.* **1989**, *94*, 11573.
- Chemical Kinetics and Photochemical Data for Use in Stratospheric Modeling: Evaluation Number 12*; DeMore, W. B., Sander, S. P., Golden, D. M., Hampson, R. F., Kurylo, M. J., Howard, C. J., Ravishankara, A. R., Kolb, C. E., Molina, M. J., Eds.; Jet Propulsion Laboratory: Pasadena, CA, 1997.
- Chemical Kinetics and Photochemical Data for Use in Stratospheric Modeling, Supplement to Evaluation 12: Update of Key Reactions*; Sander, S. P., Friedl, R. R., DeMore, W. B., Golden, D. M., Hampson, R. F., Kurylo, M. J., Hampson, R. F., Huie, R. E., Moortgat, G. K., Ravishankara, A. R., Kolb, C. E., Molina, M. J., Eds.; Jet Propulsion Laboratory: Pasadena, CA, 2000; Vol. 13.
- Lanzendorf, E. J.; Hanisco, T. F.; Stimpfle, R. M.; Anderson, J. G.; Wennberg, P. O.; Cohen, R. C. *Geophys. Res. Lett.* **2000**, accepted.
- Wamsley, P. R.; Elkins, J. W.; Fahey, D. W.; Dutton, G. S.; Volk, C. M.; Myers, R. C.; Montzka, S. A.; Butler, J. H.; Clarke, A. D.; Fraser, P. J.; Steele, L. P.; Lucarelli, M. P.; Atlas, E. L.; Schauffler, S. M.; Blake, D. R.; Rowland, F. S.; Sturges, W. T.; Lee, J. M.; Penkett, S. A.; Engel, A.; Stimpfle, R. M.; Chan, K. R.; Weisenstein, D. K.; Ko, M. K. W.; Salawitch, R. J. *J. Geophys. Res.—Atmos.* **1998**, *103*, 1513.
- Wennberg, P. O.; Hanisco, T. F.; Jaegle, L.; Jacob, D. J.; Hints, E. J.; Lanzendorf, E. J.; Anderson, J. G.; Gao, R. S.; Keim, E. R.; Donnelly, S. G.; Del Negro, L. A.; Fahey, D. W.; McKeen, S. A.; Salawitch, R. J.; Webster, C. R.; May, R. D.; Herman, R. L.; Proffitt, M. H.; Margitan, J. J.; Atlas, E. L.; Schauffler, S. M.; Flocke, F.; McElroy, C. T.; Bui, T. P. *Science* **1998**, *279*, 49.
- Jaegle, L.; Jacob, D. J.; Wennberg, P. O.; Spivakovsky, C. M.; Hanisco, T. F.; Lanzendorf, E. J.; Hints, E. J.; Fahey, D. W.; Keim, E. R.; Proffitt, M. H.; Atlas, E. L.; Flocke, F.; Schauffler, S.; McElroy, C. T.; Midwinter, C.; Pfister, L.; Wilson, J. C. *Geophys. Res. Lett.* **1997**, *24*, 3181.
- Fahey, D. W.; Kawa, S. R.; Woodbridge, E. L.; Tin, P.; Wilson, J. C.; Jonsson, H. H.; Dye, J. E.; Baumgardner, D.; Borrmann, S.; Toohey, D. W.; Avallone, L. M.; Proffitt, M. H.; Margitan, J.; Loewenstein, M.; Podolske, J. R.; Salawitch, R. J.; Wofsy, S. C.; Ko, M. K. W.; Anderson, D. E.; Schoeberl, M. R.; Chan, K. R. *Nature* **1993**, *363*, 509.
- Gao, R. S.; Fahey, D. W.; Salawitch, R. J.; Lloyd, S. A.; Anderson, D. E.; Demajst, R.; McElroy, C. T.; Woodbridge, E. L.; Wamsley, R. C.; Donnelly, S. G.; Del Negro, L. A.; Proffitt, M. H.; Stimpfle, R. M.; Kohn, D. W.; Kawa, R.; Lait, L. R.; Loewenstein, M.; Podolske, J. R.; Keim, E. R.; Dye, J. E.; Wilson, J. C.; Chan, K. R. *J. Geophys. Res.—Atmos.* **1997**, *102*, 3935.
- Stimpfle, R. M.; Koplow, J. P.; Cohen, R. C.; Kohn, D. W.; Wennberg, P. O.; Judah, D. M.; Toohey, D. W.; Avallone, L. M.; Anderson, J. G.; Salawitch, R. J.; Woodbridge, E. L.; Webster, C. R.; May, R. D.; Proffitt, M. H.; Aiken, K.; Margitan, J.; Loewenstein, M.; Podolske, J. R.; Pfister, L.; Chan, K. R. *Geophys. Res. Lett.* **1994**, *21*, 2543.
- Brune, W. H.; Tan, D.; Faloona, I. F.; Jaegle, L.; Jacob, D. J.; Heikes, B. G.; Snow, J.; Kondo, Y.; Shetter, R.; Sachse, G. W.; Anderson, B.; Gregory, G. L.; Vay, S.; Singh, H. B.; Davis, D. D.; Crawford, J. H.; Blake, D. R. *Geophys. Res. Lett.* **1999**, *26*, 3077.
- Cohen, R. C.; Perkins, K. K.; Koch, L. C.; Stimpfle, R. M.; Wennberg, P. O.; Hanisco, T. F.; Lanzendorf, E. J.; Bonne, G. P.; Voss, P. B.; Salawitch, R. J.; Del Negro, L. A.; Wilson, J. C.; McElroy, C. T.; Bui, T. P. *J. Geophys. Res.—Atmos.* **2000**, *105*, 24283.
- Del Negro, L. A.; Fahey, D. W.; Gao, R. S.; Donnelly, S. G.; Keim, E. R.; Neuman, J. A.; Cohen, R. C.; Perkins, K. K.; Koch, L. C.; Salawitch, R. J.; Lloyd, S. A.; Proffitt, M. H.; Margitan, J. J.; Stimpfle, R. M.; Bonne, G. P.; Voss, P. B.; Wennberg, P. O.; McElroy, C. T.; Swartz, W. H.; Kusterer, T. L.; Anderson, D. E.; Lait, L. R.; Bui, T. P. *J. Geophys. Res.* **1999**, *104*, 26687.
- Herndon, S. C.; Villalta, P. W.; Nelson, D. D.; Jayne, J. T.; Zahniser, M. S. *J. Phys. Chem. A*, this issue.
- Nizkorodov, S. A.; Harper, W. W.; Blackmon, B. W.; Nesbitt, D. J. *J. Phys. Chem. A* **2000**, *104*, 3964.